Light-induced agglomeration of single-atom platinum in photocatalysis

*Nikita Denisov, Shanshan Qin, Johannes Will, Bojana Nedić Vasiljevic, Natalia V. Skorodumova, Igor A. Pašti, Bidyut Bikash Sarma, Benedict Osuagwu, Tadahiro Yokosawa, Johannes Voss, Janis Wirth, Erdmann Spiecker, Patrik Schmuki**

N. Denisov, S. Qin, B. Osuagwu, P. Schmuki
Friedrich-Alexander-Universität Erlangen-Nürnberg, Department of Materials Science and Engineering, Chair for Surface Science and Corrosion (WW4-LKO), Martensstrasse 7, 91058 Erlangen, Germany
E-mail: schmuki@ww.uni-erlangen.de

J. Will, T. Yokosawa, J. Voss, J. Wirth, E. Spiecker
Friedrich-Alexander-Universität Erlangen-Nürnberg, Institute of Micro- and Nanostructure Research & Center for Nanoanalysis and Electron Microscopy (CENEM), IZNF, Cauerstraße 3, 91058 Erlangen, Germany

B. N. Vasiljevic, I. A. Pašti
Faculty of Physical Chemistry, University of Belgrade, Studentski trg 12-16, 11000 Belgrade, Serbia

N. V. Skorodumova, I. A. Pašti
Department of Materials Science and Engineering, School of Industrial Engineering and Management, KTH–Royal Institute of Technology, Brinellvägen 23, 100 44 Stockholm, Sweden

B. B. Sarma
Institute of Catalysis Research and Technology and Institute for Chemical Technology and Polymer Chemistry, Karlsruhe Institute of Technology, 76131 Karlsruhe, Germany

P. Schmuki
Regional Centre of Advanced Technologies and Materials, Šlechtitelů 27, 78371 Olomouc, Czech Republic

P. Schmuki
Department of Chemistry, Faculty of Science, King Abdulaziz University, P.O. Box 80203, Jeddah 21569, Saudi Arabia

Keywords: single-atom catalysis, Pt, TiO_2, photocatalysis, H_2 evolution

With recent advances in the field of single-atoms (SAs) used in photocatalysis, an unprecedented performance of atomically dispersed co-catalysts has been achieved. However, the stability and agglomeration of SA co-catalysts on the semiconductor surface may represent a critical issue in potential applications. Here we describe the photoinduced destabilization of Pt SAs on the benchmark photocatalyst, TiO_2. In aqueous solutions within illumination timescales ranging from few minutes to several hours, light-induced agglomeration of Pt SAs to ensembles (dimers, multimers) and finally nanoparticles takes place. The kinetics critically depends on the presence of sacrificial hole scavengers and the used light intensity. DFT calculations attribute the light induced destabilization of the SA Pt species to binding of surface-coordinated Pt with solution-hydrogen (adsorbed H atoms), which consequently weakens the Pt SA bonding to the TiO_2 surface. Despite the gradual aggregation of Pt SAs into surface clusters and their overall reduction to metallic state, which involves >90 % of Pt SAs, the overall photocatalytic H_2 evolution remains virtually unaffected.

1. Introduction

In recent years, highly dispersed species – most commonly, in the form of supported single metal atoms – have been introduced to the catalysis field with great success and high impact. Single atom catalysts (SACs) have not only lead to significant advances in heterogeneous catalysis,[1–13] but also in electrocatalysis,[14–26] as well as photocatalysis.[27–30] Photocatalytic reactions are based on a reaction sequence of *i)* the generation of photoexcited charge carriers (electron-hole pairs) in a semiconductor, *ii)* charge carrier separation and migration to the semiconductor surface, and *iii)* the reaction of the excited electrons and holes at the semiconductor surface with reactants in the environment.[31,32] A particularly important example of such a photocatalytic reaction is solar hydrogen production that can be accomplished via transfer of conduction-band electrons from a suitable semiconductor to water that then is reduced to form H_2.[33,34] While electron transfer and water reduction for many semiconductors is thermodynamically feasible, H_2 generation directly on the semiconductor

surface often occurs very sluggishly. To overcome this slow kinetics, the H_2 evolution reaction is often co-catalyzed using noble metals such as Pt, Pd, or Rh that are deposited on the semiconductor in form of nanoparticles.[33,35] The often strong acceleration of H_2 generation provided by such co-catalysts of a few nanometers in size is ascribed to a combined effect of *i)* a facilitated electron-hole separation due to the Schottky-junction at the metal/semiconductor interface and *ii)* a facilitated recombination of 2 $H^0 \rightarrow H_2$. To deposit such nanoscale noble metal particles, various techniques have been developed, most commonly based on noble metal salt precursors that are impregnated on the semiconductor surface and then are reduced chemically, thermally or photo-induced to metallic particles.[36,37] The particle loading and size can be fine-tuned to achieve a maximum co-catalytic efficiency.[38–44] To date, several studies have suggested the ideal size of the co-catalytic sites (e.g. 1 nm for Pt [45], or in contrast 0.2 nm for PtO [46]). In spite of such controversial reports, maximizing the surface to volume ratio of a co-catalytic site is most desirable not only from an efficiency- (per site or per atom) but also from an economic perspective. The maximum surface to volume ratio is achieved when the dimensions of a co-catalytic entity has reached the size of a single atom (SA). Nevertheless, as pointed out several times, for SAs, downscaling laws may no longer hold.[47] Unusual reaction pathways may become favored that may be disadvantageous or advantageous.[30,48]

Accordingly, a key issue when dealing with SAs is their stability on a chosen substrate and agglomeration is conceived to be of a paramount importance for the applicability and performance of SA catalysts.[49,50] "Stable" refers in a classic catalyst setting mainly to thermal stability, i.e. suppressing surface mobility of SAs at elevated temperatures. Many approaches to stabilizing SAs focus on a classic strong electrostatic adsorption [51] or on substrate lattice defects such as kinks, atomic steps, or often more ideally on ionic vacancies in combination with favorable surface chemistries.[1,49,50] Reliable SA trapping is regarded as a key to ensuring their stable location and catalytic reactivity, which may otherwise be disrupted by SA agglomeration at elevated temperatures.[52] In contrast to such classic thermally activated processes, in photocatalysis the activation takes place by photoinduced charge carriers but only very few SA-studies in photocatalysis report on the observation of photoinduced agglomeration of SAs to NPs.[43,53,54] Such conversion of SAs to NPs may affect the photocatalytic performance by altering the co-catalyst surface distribution, surface-to-volume ratio, and energetics of surface reactions. Correspondingly, a clear difference in the H_2 production rates by SAs and NPs has been shown in [55]. Therefore we believe that disregarding the photoinduced mobility and agglomeration of SAs may potentially lead to erroneous evaluations of their "true"

photocatalytic activity, e.g. due to the presence of "unstable" (excessive) SA sites that do not contribute significantly to the H_2 evolution, in line with previous findings [56].

Here we examine and describe in detail the photoinduced agglomeration of SAs during a photocatalytic reaction using the most classic co-catalytic/photocatalytic system: Pt on anatase TiO_2. This prototype system, loaded with various dispersed SA co-catalysts instead of NPs, has recently also attracted wide interest for photocatalytic H_2 generation from aqueous solutions, with or without sacrificial agents. TiO_2 in the form of layers,[55,57] anodic nanotubes,[58] hydrothermal nanotubes,[59] nanosheets,[55,56,60,61] nanoflakes,[62] faceted nanocrystals,[63] commercial nanoparticles,[43,64] or in the form of metal organic frameworks (MOFs),[65,66] or as black TiO_2,[67] have been investigated using SA co-catalysts.

2. Results and discussion

In order to study SA agglomeration and to trace individual surface atom movements, we use a versatile set-up that relies on SA Pt trapping on a lithographically defined thin film TiO_2 layer.[55–58,60,62] The set-up consists of a 7 nm thin anatase layer that was sputter-deposited on an 8 nm thick SiO_2 window microfabricated in a Si wafer (**Figure 1a, b; Figure S1**). The thinness of the sputter-deposited layer not only enables the conversion of the layer to the anatase polymorph of TiO_2, but more importantly provides a reliable substrate that allows high-quality imaging in an aberration-corrected high-angle annular dark-field imaging (HAADF) STEM and – even more – it allows to monitor changes in the SA configuration at identical locations [68,69] after illumination intervals.

These investigations are supplemented by investigations on single crystalline facetted anatase crystallites (nanosheets) (characterization is provided in the supporting information, **Figure S2**). To elucidate critical factors in SA stability and light induced agglomeration under photocatalytic H_2 generation conditions, all samples (thin films and nanosheets) were decorated with Pt SAs using a "dark-deposition" approach previously studied in detail [55–58,60,62] and shortly described in the experimental section. This was followed by hydrogen evolution experiments carried out under UV (λ = 365 nm) LED illumination in different aqueous solutions.

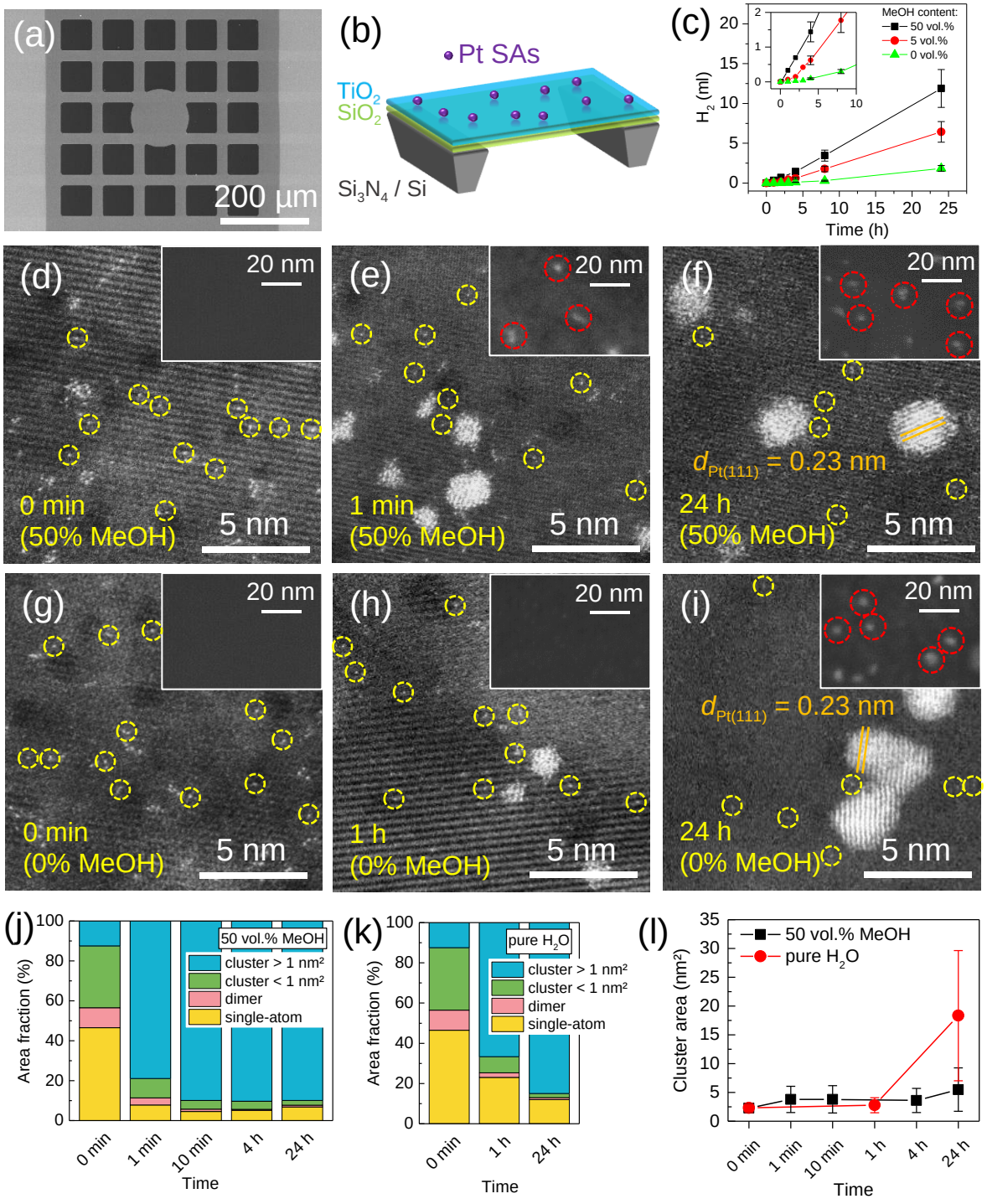

Figure 1. Characterization of Pt SA-loaded TiO_2 layers on TEM membranes. (a) Top view of a TEM membrane; (b) Schematic cross-section of a TEM membrane; (c) Photocatalytic H_2 evolution by the Pt SA-loaded TiO_2 nanosheets (2 mM H_2PtCl_6) in aqueous solutions at different MeOH concentrations; (d-f) HAADF-STEM images of TiO_2 layers after 0 min (d), 1 min (e) and 24 h (f) of irradiation (600 mW cm^{-2} at λ = 365 nm) in 50 vol.% MeOH (the insets show corresponding SEM images). (g-i) HAADF-STEM images of TiO_2 layers after 0 min (g), 1 h (h) and 24 h (i) of irradiation (65 mW cm^{-2} at λ = 365 nm) in pure water (the insets show

corresponding SEM images). (j-k) Area fraction of Pt single-atoms and clusters, and (l) average cluster area, as calculated from the HAADF-STEM images of TiO_2 layers irradiated for 0-24 h in 50 vol.% MeOH (j) or pure water (k).

Figure 1c shows the photocatalytic hydrogen evolution rates obtained from the titania anatase flakes (Pt SA-loaded in 2 mM H_2PtCl_6) in pure H_2O and in presence of a sacrificial hole capture agent (MeOH). In both cases, a linear evolution of H_2 over time is observed. The surface configuration of the Pt SAs during such an illumination process is illustrated in HAADF-STEM images of TiO_2 membranes (Pt SA-loaded in 2 mM H_2PtCl_6) before, after 1 min, and after 24 h illumination (**Figure 1d-f**), respectively. Without illumination, HAADF-STEM shows uniformly dispersed Pt atoms (either as single entity or in small ensembles). A statistical evaluation of such images via a machine learning based segmentation (an example is provided in **Figure S3**) of an average area of 5660 nm² shows that SAs are present at an average density of 4.1×10^5 µm^{-2}. In addition, three other species are identified: i) dimers, ii) small clusters classified by an area <1 nm², and iii) SA clusters with an area >1 nm². In this context, less than 13% of the Pt is agglomerated to larger clusters with an average area of ~2.3 nm² corresponding to an equivalent diameter of a circle d_e of 1.7 nm. Evidently, already after 1 min illumination (**Figure 1e**), a significant rearrangement of the surface co-catalyst can be observed. Namely, only 11% of the Pt is either in the SA or dimer form and 10% in small clusters, whereas already 79% are contained in clusters with an average size of ~3.8 nm² (d_e=2.2 nm). Finally, after 24 h illumination, the STEM visible agglomerate area increases to an average size of up to ~4-5.5 nm (d_e=2.6 nm). Notably, the fraction of SAs still takes nearly 7% of the total Pt amount. The complete statistical analysis is graphically shown in **Figure 1j** also including 10 min and 4 h illumination. The results are in-line with a first fast agglomeration of SAs and their agglomerates to larger clusters within 1 min, afterwards the fraction of SAs stabilizes and even regenerates after 10 min. In contrast, the already nucleated agglomerates dissolve or further coarsen, as evident by the size evolution of the clusters (**Figure 1l**) and discussed in more detail below. The results of HAADF imaging are complemented by chemical information from STEM EDX mapping (see **Figure S4**), which confirms a uniform Pt distribution after SA decoration, as well as formation of Pt clusters upon light exposure.

Loading with a much lower precursor concentration (0.001 mM) leads to a SA density of only 0.2×10^5 µm^{-2}, which, however, are all in a SA state (see **Figure S5**). As observed for the high concentration sample, a large fraction of these SAs agglomerate within 1 min of illumination, whereas even after 24 h still 6% of the Pt atoms are in a SA state, which means

that concentration independent nearly the same relative amount of Pt is in the SA state and agglomerated, respectively.

For the SA decorated surface, obviously the feature size is below the resolution of SEM. However, the first agglomerated clusters become SEM visible after 1 min of illumination – thus SEM allows to follow SA Pt agglomeration on larger length scales – therefore SEM images are shown in the insets of STEM images and are given again in **Figure S6**. It is noteworthy that after 24 h of illumination, the HAADF-STEM (**Figure 1f**) shows some agglomerates that can be identified as metallic crystallite nanoparticles, evident from the d-spacing of the crystallized particles – an example is shown in **Figure 1f** where d = 0.23 nm which corresponds well to the (111) plane of metallic Pt. This illustrates that SAs not only agglomerate to 2D rafts on the surface but also to 3D crystallites.

The site-specific nature of the HAADF-STEM analysis allows tracing the evolution of individual agglomerates and clusters. **Figure S7** depicts the evolution of agglomerates as function of illumination time. From 1 min to 4 h a constant change of cluster morphology can be observed, moreover the appearance of the clusters is cloudy and single spots can still be observed, this impression of a 2D object was further supported by a "defocus"-series, where the agglomerates are nearly simultaneously in focus with the substrate atoms and the surrounding SAs. Between 4 h and 24 h coarsening of the agglomerates is observed, in addition the cloudy character gets partially lost and as discussed above lattice planes can be detected implying the transformation to a 3D object. Two other examples of identical location electron microscopy are displayed in **Figure S8**, here on a larger field of view, the dissolution of a small agglomerate can be observed in a) and even cluster migration accompanied by coarsening in b). All observations point towards a high mobility of Pt atoms under photocatalytic conditions, i.e. not only Pt in the form of SAs but also Pt species that are already in an agglomerated state.

In order to confirm the general validity of the observations on the TiO_2 thin film membranes, we additionally carried out experiments on facetted TiO_2 nanosheet-powder. For this we decorated hydrothermally fabricated preferentially facetted (001) anatase nanosheet powder with Pt SAs. After synthesis (as described in the experimental section), the nanosheets were uniformly loaded with Pt SAs (see HAADF-STEM, **Figure S9a,d** and SEM, **Figure S10a**). By XPS analysis no Cl signal was detected, indicating that the precursor complex fully reacted with the surface Ti-O species. Similarly to the thin film anatase layers on the TEM-grid, already after 1 min of light exposure in 50 vol.% MeOH, aggregation of Pt SAs was observed on the dominant (001) facets of the nanosheets (**Figure S9b,e**, **Figure S10b**) and extended irradiation leads to an overall increase in size and number of Pt clusters (**Figure S9c,f**, **Figure S10c-e**).

Also in this case clusters of a crystalline metallic Pt nanoparticle can be confirmed (**Figure S9c**). The distribution of these clusters suggests that diffusion of Pt SAs takes place over the entire surface (or facets) of the nanosheets.

If the reaction medium is changed to a plain water environment, SA agglomeration and the photocatalytic reaction become significantly affected. HAADF-STEM (**Figure 1g,h,i**) shows the state of the anatase thin films after the surface has been irradiated in pure H_2O for 0 h, 1 h, and 24 h. In this case, still 23% of Pt is in a SA state and only small Pt clusters (not visible by SEM) are formed after 1 h, which is in stark contrast to the aqueous MeOH solution that shows a heavily agglomerated situation already after 1 min. In plain water, after 24 h illumination still 12% of the Pt is available in a SA state after 24 h (**Figure 1k**). Clearly, as compared to the MeOH solution, the agglomeration process is drastically slowed down in pure water.

Following consistent observations of light-induced Pt SA agglomeration on the thin sputtered TiO_2 nanolayers and the faceted anatase nanosheets, further surface analysis was performed. From the XPS data for anatase flakes (**Figure 2a,** and **Figure S10**), the Pt 4f peak shifts over the illumination time from a position of Pt $4f_{7/2}$ at 72.4 eV to 70.6 eV. A peak position for Pt $4f_{7/2}$ at ~72.4 eV corresponds well to literature data for surface coordinated single atom $Pt^{\delta+}$ with $\delta \approx 2$ [55,70] while a Pt $4f_{7/2}$ position of 70.6 eV corresponds well to Pt^0 in the form of metallic nanoparticles.[55,70] The surface reaction of the $[PtCl_6]^{2-}$ precursor leads to a reduction of the Pt^{4+} reduction to a Pt^{2+} species while all coordinating Cl^- species are lost (the latter is evident from the absence of Cl-species in the Cl 2p region XPS of a Pt SA decorated surface, **Figure S11**). Please note that the wide peak at 75.2 eV is a Ti 3s satellite peak.

In line with the microscope data, also XPS shows already after 1 min of illumination some conversion of the surface trapped $Pt^{\delta+}$ to metallic Pt^0 apparent in the spectra from the pronounced shoulder at lower binding energies, pending at ≈70-71 eV. **Figure 2b** gives an evaluation of the $Pt^{\delta+}$ and Pt^0 content over illumination time based on deconvolution of the Pt 4f signal into the two-valent and zero-valent contributions. For the data in **Figure 2a**, after 1 min, 51 % of the Pt on the surface is converted from SAs ($Pt^{\delta+}$) to Pt^0, and after 10 min of illumination, >80 % of the Pt is in a metallic state. After 24 h, 7.2% of the Pt is still in $Pt^{\delta+}$ state, which perfectly fits to the SA fraction of 7% as determined from HAADF-STEM imaging – this allows to conclude that after 24 h illumination all Pt atoms, which are not SAs are in a metallic state. This is in-line with the observed transformation of SAs to a 2D loosely bound raft to a 3D nanocrystal as described above. A comparison of the XPS and the microscopy data after 1 min reveals that at this stage a large fraction of the agglomerated Pt atoms (the rafts) is still in the $Pt^{\delta+}$ state, implying the SA binding character for SA in the small agglomerates.

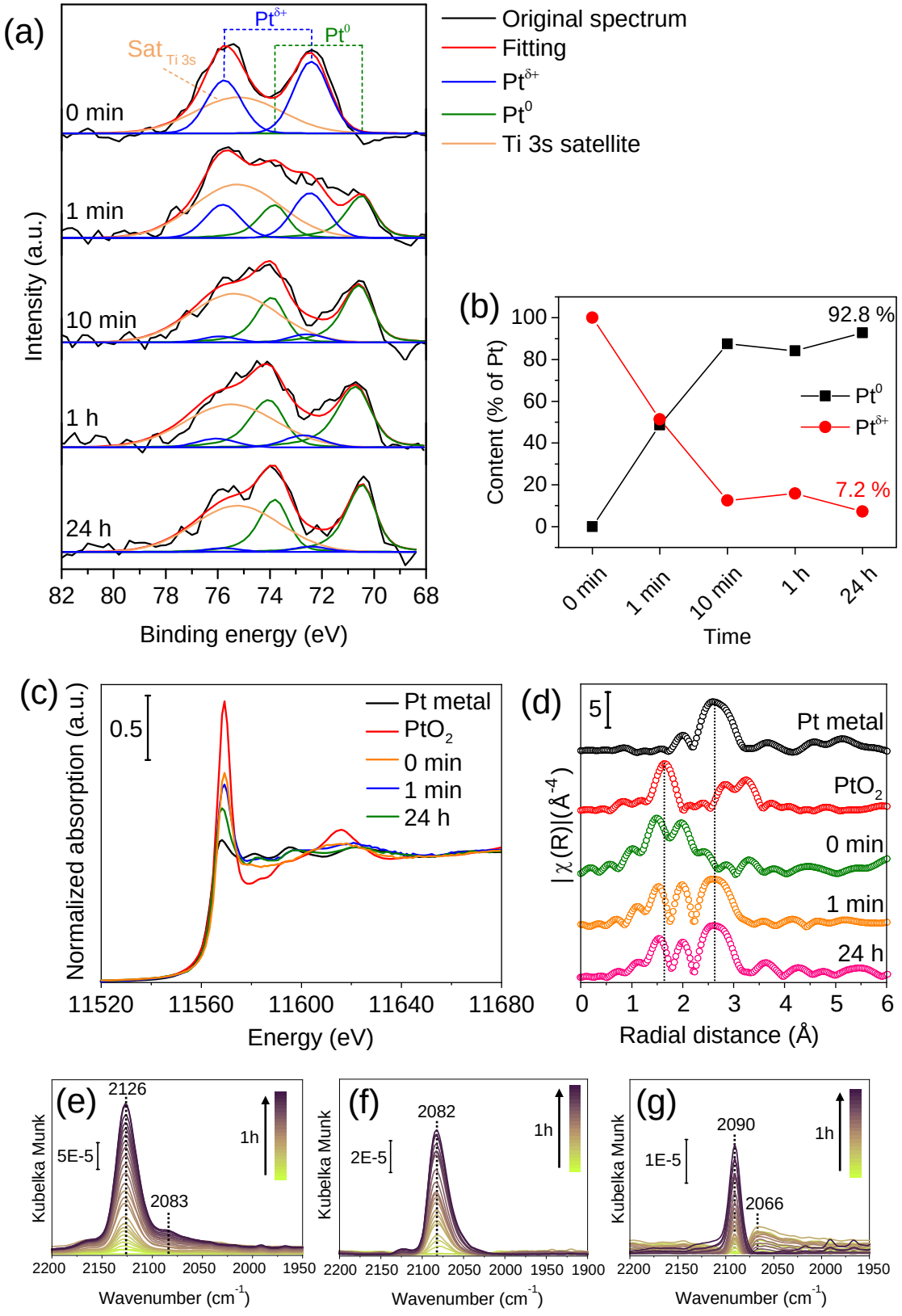

Figure 2. Characterization of the Pt SA-loaded TiO_2 nanosheets after irradiation for 0-24 h in 50 vol.% MeOH aqueous solutions. (a) Deconvoluted XPS spectra in the Pt 4f region; (b) Pt^0

and $Pt^{\delta+}$ content in the Pt species estimated from deconvoluted XPS spectra in (a). (c) Normalized XANES spectra at the Pt L_3-edge; (d) k^3-weighted FT radial distribution; (e-g) CO-DRIFT spectra after irradiation for 0 min (e), 1 min (f) and 24 h (g).

To further investigate the light induced agglomeration, we employed X-ray absorption spectroscopy (XAS) to characterize anatase nanosheet samples loaded with Pt SAs, after 1 min and 24 h of illumination in the MeOH solution (**Figure 2c,d**). The normalized X-ray absorption near edge spectra (XANES) measured at Pt L_3-edge (11.564 eV) are in accord with the presence of oxidized Pt species ($Pt^{\delta+}$), i.e. the SA deposited samples bear positively charged Pt centers similar to the Pt oxide reference as shown in **Figure 2c**. After 1 min and 24 h illumination the corresponding spectra indicate a partial reduction of the oxidized Pt species to a metallic species.

The extended X-ray absorption fine structure (EXAFS) analysis and the corresponding Fourier-transformed radial distribution function for PtO_2 reference show the presence of a Pt-O as the first shell around 1.6 Å (phase uncorrected) and the 2nd shell between 2.8-2.9 Å as shown in **Figure 2d**. Notably, Pt SA decorated nanosheets show a signal at 1.6 Å (corresponding to Pt-O) and a maximum at 1.9 Å. The signal at 1.9 Å reflects a strong interaction between Pt and the TiO_2 support via Pt-O bonds (as was reported for sub-nanometer PtO_x clusters in [71]). The samples illuminated for 1 min and 24 h show a weakened signal from Pt-O at 1.6 Å, and a characteristic peak at 2.65 Å (similarly to Pt foil reference), which is in the range of values reported for Pt-Pt bond length.[70] The k-space spectra are shown in **Figure S12** in the ESI. These findings are well in line with the crystallization of $Pt^{\delta+}$ species to Pt^0 nanoparticles observed in STEM.

XAS measurements performed for nanosheets irradiated in pure H_2O (**Figure S13**) show drastically slower rate of reduction of Pt SAs to metallic state. Here virtually no change can be seen after 1 min of irradiation, in contrast to observations in presence of MeOH.

Additional DRIFTS experiments were carried out with 1% CO diluted in Ar in a continuous flow for 1 h with a flow rate of 30 mL min^{-1}. The spectra of the non-illuminated Pt SA- anatase sheets (**Figure 2e**) show CO vibrational frequency at 2125 cm^{-1} which is characteristic of linearly bonded CO over Pt single sites.[70,72] In contrast, the samples illuminated for 1 min and 24 h, respectively, show a shift of the peak to 2082 cm^{-1} and 2090 cm^{-1} (**Figure 2f, 2g**), which is characteristic to CO adsorbed on metallic (crystalline) Pt.[70,72] Notably, slightly higher peak frequency after 24 h irradiation, as compared to 1 min, can originate from the overall higher coordination number of Pt, i.e. larger average Pt cluster size.[72] Thus XAS and DRIFTS measurements are in good agreement with TEM and XPS.

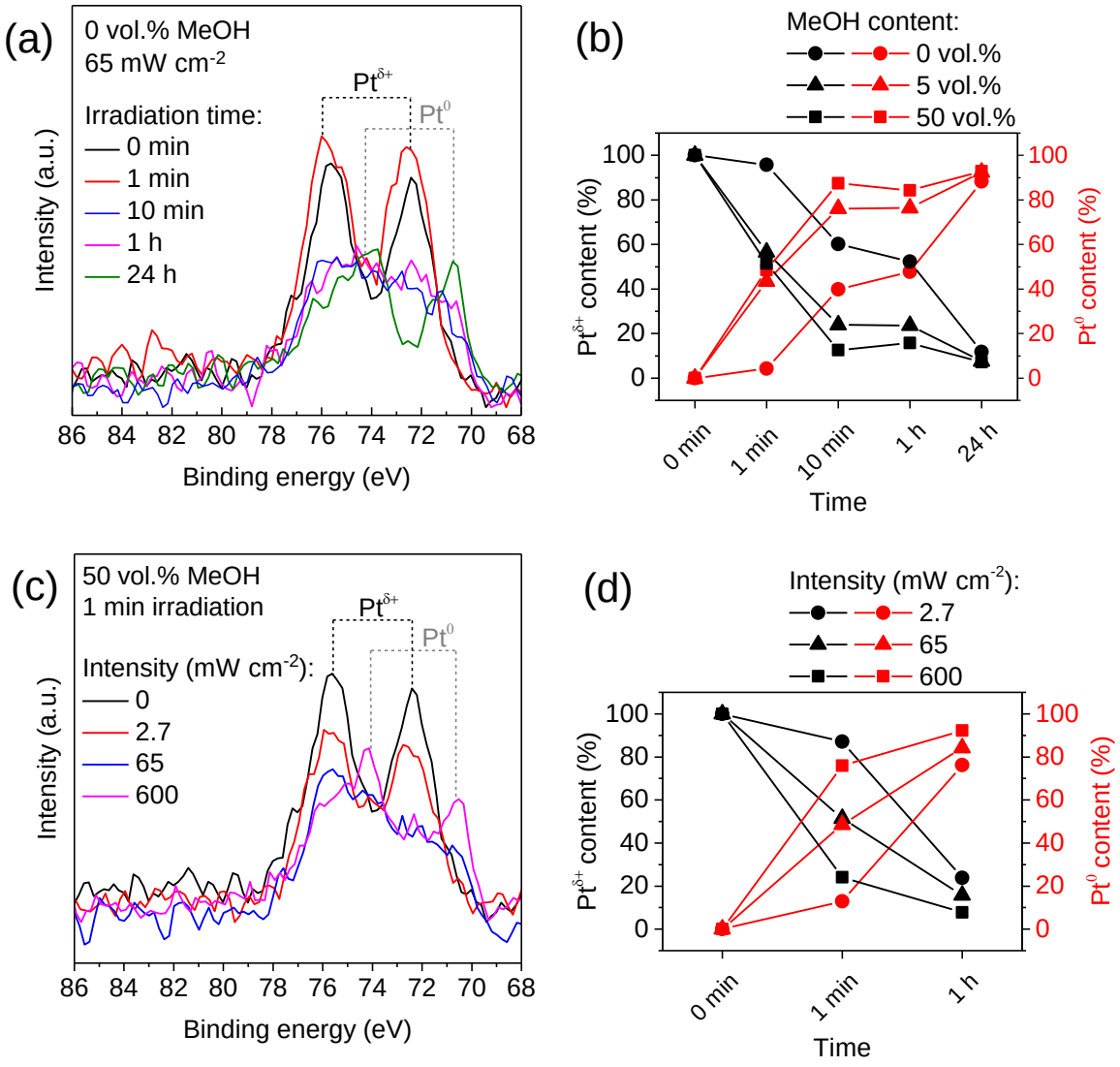

Figure 3. XPS characterization of the Pt SA-loaded TiO_2 nanosheets irradiated at different conditions. (a) XPS spectra in the Pt 4f region after irradiation in pure H_2O for different duration; (b) $Pt^{\delta+}$ and Pt^0 content evaluated from XPS spectra after irradiation in aqueous solutions with different MeOH concentrations; (c) XPS spectra in the Pt 4f region after 1 min irradiation in 50 vol.% MeOH solutions at different light intensities; (d) $Pt^{\delta+}$ and Pt^0 content evaluated from XPS spectra after irradiation in 50 vol.% MeOH solutions at different light intensities.

In order to elucidate critical factors affecting agglomeration, we further evaluated the influence of the sacrificial agent concentration (**Figure 3a,b**) and the illumination intensity (**Figure 3c,d**). From **Figure 3a,b** it is evident that already the addition of sacrificial agent (MeOH) at 5 vol.% not only strongly affects the H_2 evolution activity (**Figure 1c**) but also the agglomeration rate (**Figure 3b**). This suggests that the charge flux across the surface SAs

significantly affects the agglomeration. This is also well in line with the effect of the light intensity (**Figure 3c,d**). Evidently, with a lower light intensity, a slower agglomeration is observed. Specifically, after 1 min of irradiation at different intensities we observed 13% (at 2.7 mW cm^{-2}), 49% (at 65 mW cm^{-2}), or 76% (at 600 mW cm^{-2}) conversion of $Pt^{\delta+}$ to metallic Pt^0 (**Figure 3d**). In accordance with XPS, the corresponding SEM images (**Figure S14**) show relatively more particles on the surface for the nanosheets irradiated at higher intensities. Nevertheless, the H_2 evolution rate (**Figure S15**) remains hardly affected by the illumination for lower powers and only for intensities of >100 mW cm^{-2} show mild saturation effects. I.e., over the entire illumination intensity range the availability of charge carriers is determining the H_2 evolution rate rather than the number and availability of co-catalytic sites.

It should be noted that the light induced agglomeration is in stark contrast to the thermal stability of the SA configuration at room temperature (the XPS spectra in Pt 4f region are virtually unchanged for samples stored for 6 months at room temperature, **Figure S16a**). This suggests sufficiently high barriers for Pt SAs diffusion due to strong $Pt^{\delta+}$-TiO_2 interaction. Also illumination in dry Ar atmosphere does not lead to agglomeration (**Figure S16b**), indicating that this process requires external charge transfer pathways (e.g an aqueous reaction medium) for photogenerated charge carriers, which otherwise recombine to preserve charge neutrality.

Clearly, illumination under reaction conditions has a crucial destabilization effect on the SA configuration on the surface, as it leads to agglomeration of SAs to dimers, multimers, rafts and NPs. Based on some preliminary experiments, this apparently applies to a wider context of SA-semiconductor systems, such as Pd SA-TiO_2 and Pt SA-GaP (**Figure S17-S18**), as well as to other Pt SA deposition procedures, e.g. utilizing strong electrostatic adsorption of $(NH_3)_4PtCl_2$ and/or thermal post-treatments in air or H_2 (**Figure S19-S21**). The fact that the presence of a sacrificial hole capture agent (MeOH) leads to accelerated agglomeration indicates that an electron flux via surface anchored SAs and the follow-up reactions lead to the destabilizing effect. In other words, the reduced state of $Pt^{\delta+}$, e.g. $Pt^{(\delta-1)+}$ or Pt-H, seems to become mobile on the anatase surface. The MeOH-induced enhancement of the electron flux to Pt SA surface sites can be ascribed to the "indirect" mechanism: a swift transfer of photogenerated holes to MeOH [73,74] leads to reduced e^--h^+ recombination losses, thus allowing more electrons to reach the TiO_2 surface. In order to elucidate these findings, DFT calculations were performed. When "pristine" Pt SAs are considered on a TiO_2(100) surface, the binding is rather strong, with Pt binding energy ($E_{b,Pt}$) amounting to −5.29 eV, which is somewhat lower than Pt cohesive energy (absolute value 5.84 eV).[75] This suggests that Pt SAs could agglomerate if the Pt lattice could be restored somehow. This is supported by the fact that the

formation of Pt dimer releases an integral binding energy of −5.73 eV, and differential binding energy of −6.17 eV, which overcomes the Pt cohesive energy. In the case of TiO_2(001) surface we found SA binding energy of −6.57 eV, while dimer formation releases differential binding energy of −8.42 eV, suggesting the preference of dimer configuration over isolated SAs. The situation is similar with trimers on both surfaces, whose formation releases integral energies of −6.39 eV ((100) surface) and −7.44 eV ((001) surface). It is important to say that in the case of the (001) surface all the initial configurations of Pt SAs converged to the same final configuration, suggesting that there is a clear site preference for Pt SAs on the (001) surface.

To investigate thermodynamic driving forces for Pt SA agglomeration, we also analyzed how H binding, corresponding to the intermediate formation of Pt-H during photocatalytic H_2 evolution, affects the binding of SA Pt to the TiO_2 surface. In the case of (100) surface, the results suggest that upon H binding to Pt, the preferred binding site shifts compared to a bare Pt SA (**Figure 4a**). This goes along with an elongated Pt-surface distance or a change of the Pt SA coordination, indicating the weakening of the Pt SAs bonding to the surface (**Figure 4b,c**). The situation is the same for any Pt adsorption site investigated – once H is attached to Pt it changes the PtH binding-preference to a different adsorption site. Not only that the preferred binding site of PtH is different from that of $Pt^{\delta+}$ (the SA form), but the binding at the preferential site is also much weaker (reaching up to −1.59 eV). Thus, under H_2 evolution, H_{ads} formation at Pt SA causes the weakening of Pt binding to the TiO_2 surface and makes it more mobile over the TiO_2 surface. This is a straightforward conclusion as it was shown that the surface diffusion barriers of simple adsorbates scale with their binding energies.[76] Once the H adatom is formed on Pt SA, PtH diffuses over the surface and finds the most energetically favored site. We note that the situation is the same when one extra electron is added to the system (negatively charged slabs, see **Figure S22**). For negatively charged slabs we compared relative stability of Pt SAs at different adsorption sites and found that it perfectly correlates with the PtH binding energies at the same sites. This suggests that electron injection shifts the preferred binding sites compared to the "pristine" Pt SA. These are expected to be Pt agglomerates, as the formation of $(PtH)_2$ dimer over TiO_2 surface releases −3.27 eV, which exceeds PtH monomer binding on the surface by the factor of 2, suggesting thermodynamic preference of Pt agglomerates over Pt SAs. In the case of trimers, the formation releases −2.60 eV, which also surpasess PtH monomer binding energy significantly. The binding is favored due to the Pt-Pt interactions, which is reflected in the Pt-Pt distance in such dimer amounting to 2.47 Å (**Figure 4d,e**), being less than the corresponding interatomic distance in bulk Pt. In the case of (001) surface we found

analogous situation. PtH binding is much weaker than Pt SA binding (−2.81 eV). PtH dimer and trimer formation releases −3.64 eV and −2.71 eV, respectively.

To address the activity trends, we investigated how strongly H atoms are bonded to Pt sites on the considered TiO_2 surfaces. In the case of (001) surface, we find that SA, dimer, and trimer, all have quite similar $|\Delta G_H|$, around 0.5 eV, indicating that their activities towards H_2 formation should be similar, while the formation of agglomerates takes place under reaction conditions, due to the weakening of Pt binding to the surface and thermodynamic preference for agglomerates over isolated PtH. On the (100) surface, where we managed to stabilize Pt SAs at different adsorption sites, we found that in the case of Pt SAs there is a direct correlation between the Pt binding energy to the TiO_2 surface and the H binding energy to Pt SAs – a stronger Pt binding to the TiO_2 results in a better optimized H binding in terms of H_2 evolution (**Figure 4f**). In contrast, the H binding at Pt atoms in Pt dimer is very strong, −3.50 eV (integral binding energy), as also in trimer (−3.01 eV), suggesting that such structures do not have a high photocatalytic activity for H_2 evolution. Simply, H is bound too strongly, and the H_2 formation is not energetically favored. In contrast, the preferentially bound Pt SAs provide the best-optimized H binding in terms of the thermodynamic H_2 evolution barrier, considering different adsorption sites of Pt SAs at the anatase TiO_2(100) surface (**Figure 4g**). Thus, if the H_2 evolution on the "truly" active sites is faster than the surface diffusion of the intermediately formed PtH, such an active site remains in the SA state, while other Pt atoms will agglomerate.

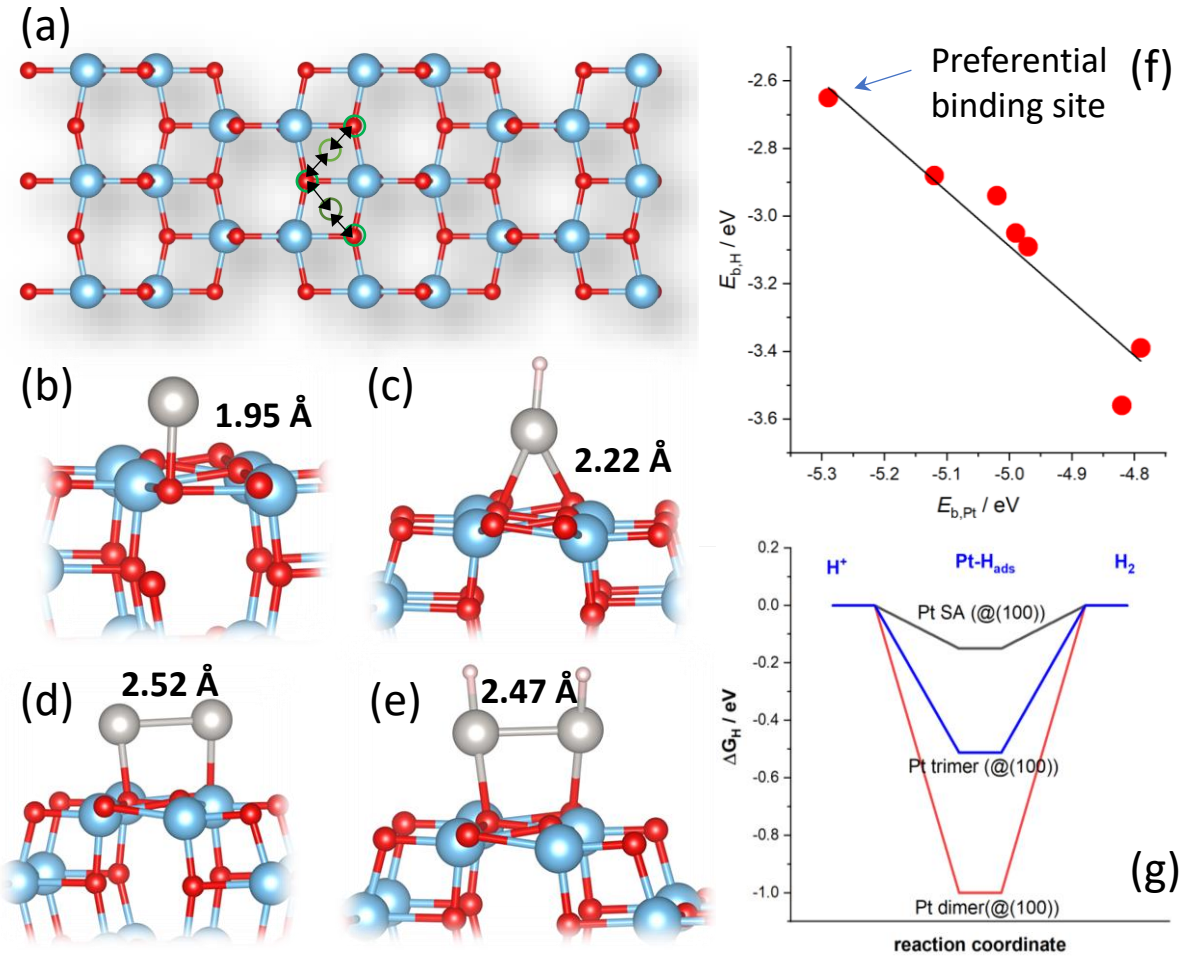

Figure 4. (a) Surface model of TiO_2(100) with indicated diffusion path of Pt SA upon formation of Hads and its release, (b) optimized structure of Pt SA on TiO_2(100), (c) optimized structure of PtH on TiO_2(100), (d) optimized structure of Pt dimer and (e) PtH dimer on TiO_2(100) surface, (f) correlation between Pt SA binding energy to the TiO_2 surface (E_b,Pt), and the H binding energy on the correspondins Pt SAs (E_b,H), (g) reaction profiles for H_2 evolution on Pt SA, Pt dimer, and Pt trimer on TiO_2(100) surface.

Based on the results of DFT calculations, the observed linearity of H_2 evolution plots (**Figure 1c**) at different MeOH concentrations (despite the apparent formation of less active agglomeration rates) can be now ascribed to the predominant H_2 production by light-stable SA sites, whereas the contribution from mobile Pt species forming clusters and nanoparticles has an apparently small impact on the overall performance (in line with [56]). Notably, stable H_2 evolution rates even at the initial 0–1 h of irradiation (which corresponds to incomplete agglomeration in pure water) may indicate that the formation of inactive Pt species (e.g. Pt dimers) occurs at a time scale smaller than the resolution of the measured H_2 evolution plots. This is supported by observations of abundant nanoparticles formed already during the initial 1

min of irradiation in 50 vol.% MeOH (**Figure 1e**). Although the stable $Pt^{\delta+}$ sites constitute less than 10 % of the total surface Pt (according to XPS analysis after 24 h of irradiation in **Figure 2b**), we suggest that these sites can yield the majority of H_2 owing to the superior surface coverage and favorable energetics of H-bonding.

3. Conclusion

The present study provides an important insight on the matter of stability of Pt SAs on TiO_2 surfaces over the course of photocatalytic H_2 evolution. Initiating photocatalytic reactions triggers surface migration and agglomeration of otherwise stable Pt SAs, which in our case affects >90% of the loaded Pt SAs on both thin film TiO_2 layers and hydrothermal TiO_2 nanosheets. Notably stable H_2 evolution rates measured for different light intensities over 24 h lead us to identify charge carriers rather than the availability of co-catalytic sites as rate-determining quantity and accordingly, the observed agglomeration behavior is independent of the initial SA loading and does not affect the overall reaction rate. Agglomeration can be subdivided into three stages i) initial fast agglomeration of SAs and dimers to loosely bound 2D rafts, ii) further agglomeration to 3D nanocrystals, and iii) slow ripening of the 3D nanocrystals. Further, we observe at least 6% of the initially loaded SAs in a SA state and could identify $Pt^{\delta+}$ states being present in the 2D rafts. The distinct correlation of the agglomeration rate with the presence of hole scavenger or irradiation intensity, points out that the agglomeration process is driven by photogenerated electrons, and their transfer to the surface Pt-atoms. DFT calculations point out the significant weakening of Pt SA bonding to TiO_2 surface upon adsorption of H atoms which leads to surface migration of PtH units and finally to the agglomeration of the Pt co-catalyst species.

4. Experimental Section

Materials: 8 nm SiO_2 membranes with 200 nm Si_3N_4 mesh on 200 µm silicon (Ted Pella, Inc., and PELCO International) were purchased from Plano Gmbh. $Ti(OBu)_4$ (98 %, Sigma-Aldrich), HF (47 %, Carl Roth), $H_2PtCl_6 \cdot 6H_2O$ (Metakem), methanol (MeOH, 99.9 %, Carl Roth) were used as received without additional purification.

Fabrication of TiO_2 supports: 7 nm thick TiO_2 films were sputtered on the 8 nm SiO_2 membranes by magnetron sputtering, followed by annealing in air at 450°C for 1 h.

TiO_2 nanosheets with dominant (001) facets were synthesized via hydrothermal route. First, 1.2 mL HF was added dropwise to 10 mL of $Ti(OBu)_4$ and vigorously stirred for 40 min at room temperature. The solution was then sealed in a Teflon-lined autoclave and heated to 200°C in an oven. After 24 h of heat treatment, the autoclave was cooled naturally, and the precipitated reaction products were collected by centrifuging and washed with ethanol and deionized water (this sequence was repeated for 3 times). The obtained powders were dried in air at 75 °C for 24 h.

Pt SA-loading on TiO_2 supports: Pt SAs were loaded on the surface of TiO_2 supports by a facile dark deposition/impregnation method.[55–58,60,62] TiO_2 films on supporting membranes were immersed in 100 ml of an aqueous solution of $H_2PtCl_6 \cdot 6H_2O$ for 1 h. The membranes were washed with deionized water and dried in N_2 gas flow.

Similarly, 20 mg of TiO_2 nanosheets were dispersed in an aqueous solution of $H_2PtCl_6 \cdot 6H_2O$ (concentration range of 0.0005–2 mM), followed by stirring in dark at room temperature for 24 h. The suspensions were then centrifuged, and the collected powders were washed with deionized water (this sequence was repeated for 3 times). The obtained powders were dried in air at 70°C for 24 h.

HAADF-STEM imaging: Identical location high-angle annular dark-field transmission electron microscopy (HAADF-STEM) images were acquired with a Thermo Fisher Scientific Spectra 200 C-FEG. The microscope is probe-corrected and equipped with a cold field emission gun (X-CFEG). Images were taken at 200 kV with dwell times between 5 and 40 µs, a collection angle of 56-200 mrad and a beam current below 20 pA.

Machine learning-based segmentation of HAADF-STEM images: Machine learning-based segmentation was performed with the commercial software Arivis Vision 4D (version 3.2). The software employs a random forest classifier-based algorithm based on "Ilastik" [77] to separate regions with and without SAs present. This advanced procedure allows segmentation not only based on image grey-values (intensity), but also on edge properties, texture and localization in the 2D image. In a second step, the generated segments are classified, corresponding to their calculated area, as SA (< 0.11 nm^2), dimer (0.11-0.16 nm^2), cluster < 1 nm^2 (0.16-1.0 nm^2) and cluster > 1 nm^2 structures (>1.0 nm^2). Finally, the estimated area occupied by each type of Pt structures is divided by their total area to obtain the corresponding area fraction values.

Morphology and composition characterization: The surface morphology of Pt SA-loaded TiO_2 supports before and after irradiation was characterized by field-emission scanning electron microscopy (SEM, Hitachi S-4800), transmission electron microscopy (TEM, Philips CM30). The chemical composition was studied by X-ray photoelectron spectroscopy (XPS, PHI 5600). The specific surface area of TiO_2 nanosheets was measured by Brunauer-Emmett-Teller (BET) method. Pt content in Pt SA-loaded TiO_2 nanosheets was determined by electrothermal atomization atomic absorption spectroscopy (ETA-AAS, Analytik Jena AG contrAA® 600) using a high-resolution double monochromator and Xe light source.

X-ray absorption spectra were collected at P65 (Petra III) beamline at the Deutsches Elektronen-Synchrotron (DESY) Hamburg, Germany. All the spectra were measured at Pt L_3-edge (11.564 eV) using a Si(111) double crystal monochromator to scan the incident energy. The energy was calibrated with a reference platinum metal foil. The measurements were conducted in transmission mode (reference samples were diluted with cellulose and pressed in a pellet) and in fluorescence mode (as a powder in a quartz capillary without any dilution). Fluorescence X-rays were collected using a 4 pixel silicon drift detector (SDD).

Diffuse reflectance infra-red spectroscopy (DRIFTS) measurements were carried out on a VERTEX 70 FTIR spectrometer (Bruker) in a Harrick *in-situ* diffuse reflectance cell. The cell was covered with a CaF_2 window. Prior to measurements, the catalysts were sieved to a size of 100-200 μm. Firstly, the catalysts were purged with Ar via mass flow controller and heated to 353 K to remove weakly bound impurities over a time period of 1 hour. The spectra were collected in reflectance (R) mode under 1% CO/Ar gas flow at room temperature in the range of 1000-4000 cm^{-1} with spectral resolution of 6 cm^{-1}. The measurements were performed continuously with a the duration of 1 hour. 200 scans were collected for background spectra (under Ar flow) and 150 scans were collected for the measurement of each sample. The composition of the gas mixture was constantly monitored by a quadrupole mass spectrometer. The recorded spectra are reported in Kubelka-Munk (KM) units by converting the reflectance by the following equation:

$$KM = \frac{(1-R)^2}{2R} \quad (1)$$

Photocatalytic H_2 evolution: Photocatalytic H_2 evolution by Pt SA-loaded nanosheets was studied at different light intensities in absence or presence of a hole scavenger (MeOH). 2 mg of powders were ultrasonically dispersed in 10 ml aqueous MeOH solutions, purged with Ar gas for 20 min, and irradiated under vigorous stirring in sealed quartz cells using LED light source (λ_{max} = 365 nm, I_{max} = 600 mW cm^{-2}). The concentration of H_2 gas produced in the cells

was measured by gas chromatograph (Shimadzu GCMS-QO2010SE) over different periods of irradiation time. The powders were then collected by centrifuging and dried in air at 70°C. TEM membranes were irradiated under the same conditions (non-TiO_2 surfaces were protected with Parafilm tape) over different periods of time, following by drying under N_2 gas flow.

DFT calculations: Density Functional Theory (DFT) calculations were done using QUANTUM ESPRESSO software.[78] Calculations were done at the GGA-PBE level.[79] The kinetic energy cut-off for the plane-wave basis set was 50 Ry, while the charge density cut-off was set to 800 Ry. Atomic positions were relaxed until the residual forces acting on atoms were below 0.01 eV $Å^{-1}$. Anatase (100) slab was created using a 2×2 supercell containing 120 atoms, following the addition of 20 Å of vacuum to generate the desired surface plane. The (001) surface was modelled using 3×3 surface cell with 108 atoms in the pristine slab. The first irreducible Brillouin zone was sampled with a 2×2×1 set of k-points generated using the general Monkhorst-Pack scheme.[80] In the first step, Pt adsorption was investigated on different adsorption sites on the TiO_2 surface. Pt binding ($E_{b,Pt}$) energy was calculated as:

$$E_{\mathrm{b,Pt}} = E_{\mathrm{Pt@TiO_2}} - \left(E_{\mathrm{TiO_2}} + E_{\mathrm{Pt}}\right) \quad (2)$$

where $E_{\mathrm{Pt@TiO_2}}$, $E_{\mathrm{TiO_2}}$, and E_{Pt}, are the total energy of the TiO_2 slab with Pt adatom, the total energy of the TiO_2 slab, and the total energy of an isolated Pt atom.

H binding energy at Pt atoms and the binding energy of the PtH fragment to the TiO_2 surface were calculated in an analogous way following Eq. (2). In the case of Pt dimer (n = 2) and trimer (n = 3), differential and integral binding energies were obtained using the following equations:

$$E_{\mathrm{b,Pt}}{}^{int} = \left(E_{\mathrm{Pt_2@TiO_2}} - \left(E_{\mathrm{TiO_2}} + nE_{\mathrm{Pt}}\right)\right)/n \quad (3)$$

$$E_{\mathrm{b,Pt}}{}^{diff} = E_{n\mathrm{Pt_2@TiO_2}} - \left(E_{(n-1)\mathrm{Pt@TiO_2}} + E_{\mathrm{Pt}}\right) \quad (4)$$

Analogous calculations were done for the $(PtH)_2$ dimer and $(PtH)_3$ trimer. Further, to convert hydrogen binding energies on Pt to Gibbs free energies of H_{ads} formation (ΔG_H), in terms of H_2 evolution, the procedure of Nørskov et al. was used.[81] The obtained structures were visualized using VESTA software.[82]

Statistical analysis: Experimental data processing was performed using the Origin software. No statistical analysis was performed for the SEM, XPS, XANES, EXAFS, CO-DRIFT data. The reproducibility of morphology and composition of the as-formed Pt SA-loaded samples was

confirmed by SEM and XPS in at least 3 experiments. Photocatalytic H_2 evolution curves were measured in single experiment with error bars corresponding to a typical range of experimental error. Statistical analysis of the area fraction and the cluster area of the surface Pt after different illumination periods was performed by calculating mean average of the values obtained by machine learning-based segmentation of HAADF-STEM images taken in 4 different locations of the sample with the total area of 5660 nm², and the standard deviation is represented by the error bars. XPS spectra were pre-processed, analyzed and fitted using a PHI Multipak software. Pre-processing of the XPS spectra included shifting to a standard Ti 2p peak position in TiO_2 at 458.5 eV and smoothening. Fitting of the XPS spectra was performed using a Shirley background with symmetric $Pt^{\delta+}$, asymmetric Pt^0, and Ti 3s satellite peaks until reaching convergence (Chi-Squared value below 5). XAS data reduction was carried out using the Demeter software packages. Data reduction (alignment and normalization) was accomplished using the Athena code (version 0.9.26).[83]

Supporting Information

Supporting Information is available from the Wiley Online Library or from the author.

Acknowledgements

The authors would like to acknowledge DFG and the Operational Program Research, Development and Education (European Regional Development Fund, Project No. CZ.02.1.01/0.0/0.0/15_003/0000416 of the Ministry of Education, Youth and Sports of the Czech Republic) for financial support. The authors would like to thank Dr. Edmund Welter, beamline scientist of P65 (DESY, Hamburg) and Dr. Dmitry Doronkin, KIT for their assistance in setting up the beamline. Ja.Wi., Jo.Wi. and E.S. acknowledge the research training group GRK 1896 “In Situ Microscopy with Electrons, X-rays, and Scanning Probes”. I.A.P. acknowledges the support from the Science Fund of the Republic of Serbia (PROMIS programme, RatioCAT, no. 606224). The computations and computational data handling were enabled by resources provided by the Swedish National Infrastructure for Computing (SNIC) at the NSC center of Linköping University, partially funded by the Swedish Research Council through grant agreement no. 2018-05973.

Conflict of Interest

The authors declare no conflict of interest.

Data Availability Statement

The data that supports the findings of this study are available within the article and its supplementary material.

Received: ((will be filled in by the editorial staff))
Revised: ((will be filled in by the editorial staff))
Published online: ((will be filled in by the editorial staff))

References

[1] Y. Chen, S. Ji, C. Chen, Q. Peng, D. Wang, Y. Li, *Joule* **2018**, *2*, 1242.
[2] H. Zhang, G. Liu, L. Shi, J. Ye, *Adv. Energy Mater.* **2018**, *8*, 1701343.
[3] S. Mitchell, J. Pérez-Ramírez, *Nat. Commun.* **2020**, *11*, 4302.
[4] Y. Shang, X. Xu, B. Gao, S. Wang, X. Duan, *Chem. Soc. Rev.* **2021**, *50*, 5281.
[5] Z. Li, S. Ji, Y. Liu, X. Cao, S. Tian, Y. Chen, Z. Niu, Y. Li, *Chem. Rev.* **2020**, *120*, 623.
[6] X. Yang, A. Wang, B. Qiao, J. Li, J. LIU, T. ZHANG, *Acc. Chem. Res.* **2013**, *46*, 1740.
[7] S. Liang, C. Hao, Y. Shi, *ChemCatChem* **2015**, *7*, 2559.
[8] S. Ding, M. J. Hülsey, J. Pérez-Ramírez, N. Yan, *Joule* **2019**, *3*, 2897.
[9] M. B. Gawande, P. Fornasiero, R. Zbořil, *ACS Catal.* **2020**, *10*, 2231.
[10] D. Liu, Q. He, S. Ding, L. Song, *Adv. Energy Mater.* **2020**, *10*, 2001482.
[11] X. Li, Y. Huang, B. Liu, *Chem* **2019**, *5*, 2733.
[12] S. K. Kaiser, Z. Chen, D. Faust Akl, S. Mitchell, J. Pérez-Ramírez, *Chem. Rev.* **2020**, *120*, 11703.
[13] B. C. Gates, M. Flytzani-Stephanopoulos, D. A. DIxon, A. Katz, *Catal. Sci. Technol.* **2017**, *7*, 4259.
[14] Y. Zhang, L. Guo, L. Tao, Y. Lu, S. Wang, *Small Methods* **2019**, *3*, 1800406.
[15] H. Fei, J. Dong, D. Chen, T. Hu, X. Duan, I. Shakir, Y. Huang, X. Duan, *Chem. Soc. Rev.* **2019**, *48*, 5207.
[16] J. Su, R. Ge, Y. Dong, F. Hao, L. Chen, *J. Mater. Chem. A* **2018**, *6*, 14025.
[17] Y. Wang, D. Wang, Y. Li, *Adv. Mater.* **2021**, *33*, 2008151.

[18] S. Chen, M. Cui, Z. Yin, J. Xiong, L. Mi, Y. Li, *ChemSusChem* **2021**, *14*, 73.

[19] B. Lu, Q. Liu, S. Chen, *ACS Catal.* **2020**, *10*, 7584.

[20] J. Han, J. Bian, C. Sun, *Research* **2020**, *2020*, 1.

[21] B. Zhang, B. Zhang, Y. Jiang, T. Ma, H. Pan, W. Sun, *Small* **2021**, *17*, 2101443.

[22] W. Zang, Z. Kou, S. J. Pennycook, J. Wang, *Adv. Energy Mater.* **2020**, *10*, 1903181.

[23] K. Kamiya, *Chem. Sci.* **2020**, *11*, 8339.

[24] Y. Zhou, J. Li, X. Gao, W. Chu, G. Gao, L.-W. Wang, *J. Mater. Chem. A* **2021**, *9*, 9979.

[25] Q. Zhang, J. Guan, *Adv. Funct. Mater.* **2020**, *30*, 2000768.

[26] C. Zhu, S. Fu, Q. Shi, D. Du, Y. Lin, *Angew. Chemie - Int. Ed.* **2017**, *56*, 13944.

[27] Q. Zhang, J. Guan, *Sol. RRL* **2020**, *4*, 2000283.

[28] Q. Wang, D. Zhang, Y. Chen, W.-F. Fu, X.-J. Lv, *ACS Sustain. Chem. Eng.* **2019**, *7*, 6430.

[29] J. Fu, S. Wang, Z. Wang, K. Liu, H. Li, H. Liu, J. Hu, X. Xu, H. Li, M. Liu, *Front. Phys.* **2020**, *15*, 28.

[30] F. Zhang, Y. Zhu, Q. Lin, L. Zhang, X. Zhang, H. Wang, *Energy Environ. Sci.* **2021**, *14*, 2954.

[31] A. O. Ibhadon, P. Fitzpatrick, *Catalysts* **2013**, *3*, 189.

[32] J. Schneider, M. Matsuoka, M. Takeuchi, J. Zhang, Y. Horiuchi, M. Anpo, D. W. Bahnemann, *Chem. Rev.* **2014**, *114*, 9919.

[33] X. Chen, S. Shen, L. Guo, S. S. Mao, *Chem. Rev.* **2010**, *110*, 6503.

[34] A. J. Bard, *J. Photochem.* **1979**, *10*, 59.

[35] S. Bai, W. Yin, L. Wang, Z. Li, Y. Xiong, *RSC Adv.* **2016**, *6*, 57446.

[36] K. Wenderich, G. Mul, *Chem. Rev.* **2016**, *116*, 14587.

[37] Y. Xu, L. Chen, X. Wang, W. Yao, Q. Zhang, *Nanoscale* **2015**, *7*, 10559.

[38] C. Dong, C. Lian, S. Hu, Z. Deng, J. Gong, M. Li, H. Liu, M. Xing, J. Zhang, *Nat. Commun.* **2018**, *9*, 1.

[39] I. Vamvasakis, B. Liu, G. S. Armatas, *Adv. Funct. Mater.* **2016**, *26*, 8062.

[40] J. Ma, X. Tan, Q. Zhang, Y. Wang, J. Zhang, L. Wang, *ACS Catal.* **2021**, *11*, 3352.

[41] Y. Ben-Shahar, F. Scotognella, I. Kriegel, L. Moretti, G. Cerullo, E. Rabani, U. Banin, *Nat. Commun.* **2016**, *7*, 1.

[42] F. Xue, C. Chen, W. Fu, M. Liu, C. Liu, P. Guo, S. Shen, *J. Phys. Chem. C* **2018**, *122*, 25165.

[43] C. Dessal, L. Martínez, C. Maheu, T. Len, F. Morfin, J. L. Rousset, E. Puzenat, P.

Afanasiev, M. Aouine, L. Soler, J. Llorca, L. Piccolo, *J. Catal.* **2019**, *375*, 155.

[44] D. Riassetto, C. Holtzinger, M. Langlet, *J. Mater. Sci.* **2009**, *44*, 2637.

[45] D. Wang, Z. P. Liu, W. M. Yang, *ACS Catal.* **2018**, *8*, 7270.

[46] Y. H. Li, J. Xing, X. H. Yang, H. G. Yang, *Chem. - A Eur. J.* **2014**, *20*, 12377.

[47] S. Gutić, A. Dobrota, E. Fako, N. Skorodumova, N. López, I. Pašti, *Catalysts* **2020**, *10*, 290.

[48] C. Gao, J. Low, R. Long, T. Kong, J. Zhu, Y. Xiong, *Chem. Rev.* **2020**, *120*, 12175.

[49] H. Hu, J. Wang, P. Tao, C. Song, W. Shang, T. Deng, J. Wu, *J. Mater. Chem. A* **2022**, *10*, 5835.

[50] Y. Chen, Z. Huang, Z. Ma, J. Chen, X. Tang, *Catal. Sci. Technol.* **2017**, *7*, 4250.

[51] M. Schreier, J. R. Regalbuto, *J. Catal.* **2004**, *225*, 190.

[52] J. Jones, H. Xiong, A. T. DeLaRiva, E. J. Peterson, H. Pham, S. R. Challa, G. Qi, S. Oh, M. H. Wiebenga, X. I. Pereira Hernández, Y. Wang, A. K. Datye, *Science* **2016**, *353*, 150.

[53] X. Zhou, I. Hwang, O. Tomanec, D. Fehn, A. Mazare, R. Zboril, K. Meyer, P. Schmuki, *Adv. Funct. Mater.* **2021**, *31*, 2102843.

[54] L. Liu, D. M. Meira, R. Arenal, P. Concepcion, A. V. Puga, A. Corma, *ACS Catal.* **2019**, *9*, 10626.

[55] S. Hejazi, S. Mohajernia, B. Osuagwu, G. Zoppellaro, P. Andryskova, O. Tomanec, S. Kment, R. Zbořil, P. Schmuki, *Adv. Mater.* **2020**, *32*, 1908505.

[56] S. Qin, N. Denisov, J. Will, J. Kolařík, E. Spiecker, P. Schmuki, *Sol. RRL* **2022**, 6, 2101026.

[57] Y. Wang, I. Hwang, Z. Wu, P. Schmuki, *Electrochem. commun.* **2021**, *133*, 107166.

[58] Z. Wu, I. Hwang, G. Cha, S. Qin, O. Tomanec, Z. Badura, S. Kment, R. Zboril, P. Schmuki, *Small* **2022**, *18*, 2104892.

[59] Y. Chen, S. Ji, W. Sun, Y. Lei, Q. Wang, A. Li, W. Chen, G. Zhou, Z. Zhang, Y. Wang, L. Zheng, Q. Zhang, L. Gu, X. Han, D. Wang, Y. Li, *Angew. Chemie - Int. Ed.* **2020**, *59*, 1295.

[60] G. Cha, I. Hwang, S. Hejazi, A. S. Dobrota, I. A. Pašti, B. Osuagwu, H. Kim, J. Will, T. Yokosawa, Z. Badura, Š. Kment, S. Mohajernia, A. Mazare, N. V. Skorodumova, E. Spiecker, P. Schmuki, *iScience* **2021**, *24*, 102938.

[61] X. Hu, J. Song, J. Luo, H. Zhang, Z. Sun, C. Li, S. Zheng, Q. Liu, *J. Energy Chem.* **2021**, *62*, 1.

[62] G. Cha, A. Mazare, I. Hwang, N. Denisov, J. Will, T. Yokosawa, Z. Badura, G.

Zoppellaro, A. B. Tesler, E. Spiecker, P. Schmuki, *Electrochim. Acta* **2022**, *412*, 140129.

[63] T. Wei, Y. Zhu, Y. Wu, X. An, L.-M. Liu, *Langmuir* **2019**, *35*, 391.

[64] L. DeRita, J. Resasco, S. Dai, A. Boubnov, H. V. Thang, A. S. Hoffman, I. Ro, G. W. Graham, S. R. Bare, G. Pacchioni, X. Pan, P. Christopher, *Nat. Mater.* **2019**, *18*, 746.

[65] T. Wang, X. Tao, X. Li, K. Zhang, S. Liu, B. Li, *Small* **2021**, *17*, 2006255.

[66] Y. Zhang, J. Zhao, H. Wang, B. Xiao, W. Zhang, X. Zhao, T. Lv, M. Thangamuthu, J. Zhang, Y. Guo, J. Ma, L. Lin, J. Tang, R. Huang, Q. Liu, *Nat. Commun.* **2022**, *13*, 58.

[67] T. Wang, Y. Zhu, Z. Luo, Y. Li, J. Niu, C. Wang, *Environ. Chem. Lett.* **2021**, *19*, 1815.

[68] N. Hodnik, G. Dehm, K. J. J. Mayrhofer, *Acc. Chem. Res.* **2016**, *49*, 2015.

[69] K. J. J. Mayrhofer, J. C. Meier, S. J. Ashton, G. K. H. Wiberg, F. Kraus, M. Hanzlik, M. Arenz, *Electrochem. commun.* **2008**, *10*, 1144.

[70] Q. Liu, Z. Zhang, *Catal. Sci. Technol.* **2019**, *9*, 4821.

[71] X. Cheng, Y. Li, L. Zheng, Y. Yan, Y. Zhang, G. Chen, S. Sun, J. Zhang, *Energy Environ. Sci.* **2017**, *10*, 2450.

[72] H. V. Thang, G. Pacchioni, L. DeRita, P. Christopher, *J. Catal.* **2018**, *367*, 104.

[73] Z. H. N. Al-azri, W.-T. Chen, A. Chan, V. Jovic, T. Ina, H. Idriss, G. I. N. Waterhouse, *J. Catal.* **2015**, *329*, 355.

[74] M. J. Berr, P. Wagner, S. Fischbach, A. Vaneski, J. Schneider, A. S. Susha, A. L. Rogach, F. Jäckel, J. Feldmann, *Appl. Phys. Lett.* **2012**, *100*, 223903.

[75] C. Kittel, *Introduction to Solid State Physics*, *8th Edition*, Wiley, **2004**.

[76] A. U. Nilekar, J. Greeley, M. Mavrikakis, *Angew. Chemie Int. Ed.* **2006**, *45*, 7046.

[77] C. Sommer, C. Straehle, U. Kothe, F. A. Hamprecht, in *2011 IEEE Int. Symp. Biomed. Imaging From Nano to Macro*, IEEE, **2011**, pp. 230–233.

[78] P. Giannozzi, S. Baroni, N. Bonini, M. Calandra, R. Car, C. Cavazzoni, D. Ceresoli, G. L. Chiarotti, M. Cococcioni, I. Dabo, A. Dal Corso, S. de Gironcoli, S. Fabris, G. Fratesi, R. Gebauer, U. Gerstmann, C. Gougoussis, A. Kokalj, M. Lazzeri, L. Martin-Samos, N. Marzari, F. Mauri, R. Mazzarello, S. Paolini, A. Pasquarello, L. Paulatto, C. Sbraccia, S. Scandolo, G. Sclauzero, A. P. Seitsonen, A. Smogunov, P. Umari, R. M. Wentzcovitch, *J. Phys. Condens. Matter* **2009**, *21*, 395502.

[79] J. P. Perdew, K. Burke, M. Ernzerhof, *Phys. Rev. Lett.* **1996**, *77*, 3865.

[80] K. Hu, M. Wu, S. Hinokuma, T. Ohto, M. Wakisaka, J. Fujita, Y. Ito, *J. Mater. Chem. A* **2019**, *7*, 2156.

[81] J. K. Nørskov, T. Bligaard, A. Logadottir, J. R. Kitchin, J. G. Chen, S. Pandelov, U.

Stimming, *J. Electrochem. Soc.* **2005**, *152*, J23.

[82] K. Momma, F. Izumi, *J. Appl. Crystallogr.* **2011**, *44*, 1272.

[83] B. Ravel, M. Newville, *J. Synchrotron Radiat.* **2005**, *12*, 537.